

KMC-1: A high resolution and high flux soft x-ray beamline at BESSY

F. Schaefers, M. Mertin, and M. Gorgoi
 BESSY GmbH, Albert-Einstein-Strasse 15, 12489 Berlin, Germany

(Received 6 September 2007; accepted 16 October 2007; published online 4 December 2007)

The crystal monochromator beamline KMC-1 at a BESSY II bending magnet covers the energy range from soft (1.7 keV) to hard x-rays (12 keV) employing the ($n, -n$) double crystal arrangement with constant beam offset. The monochromator is equipped with three sets of crystals, InSb, Si (111), and Si (422) which are exchangeable *in situ* within a few minutes. Beamline and monochromator have been optimized for high flux and high resolution. This could be achieved by (1) a windowless setup under ultrahigh-vacuum conditions up to the experiment, (2) by the use of only three optical elements to minimize reflection losses, (3) by collecting an unusually large horizontal radiation fan (6 mrad) with the toroidal premirror, and (4) the optimization of the crystal optics to the *soft* x-ray range necessitating quasibackscattering crystal geometry ($\theta_{\text{Bragg,max}}=82^\circ$) delivering crystal limited resolution. The multipurpose beamline is in use for a variety of user facilities such as extended x-ray absorption fine structure, ((Bio-)EXAFS) near-edge x-ray absorption fine structure (NEXAFS), absorption and fluorescence spectroscopy. Due to the windowless UHV setup the k edges of the technologically and biologically important elements such as Si, P, and S are accessible. In addition to these experiments this beamline is now extensively used for photoelectron spectroscopy at high kinetic energies. Photon flux in the 10^{11} – 10^{12} photons/s range and beamline resolving powers of more than $E/\Delta E \approx 100.000$ have been measured at selected energies employing Si (nnn) high order radiation in quasibackscattering geometry, thus photoelectron spectroscopy with a total instrumental resolution of about 150 meV is possible. This article describes the design features of the beamline and reports some experimental results in the above mentioned fields. © 2007 American Institute of Physics. [DOI: 10.1063/1.2808334]

I. INTRODUCTION

With a ring energy of 1.7 GeV the third generation storage ring BESSY II has been optimized for the production of vacuum ultraviolet (VUV) and *soft* x-ray radiation. This range is extensively covered by undulators employing permanent magnet technology.^{1–3} These undulators deliver polarized high brilliance radiation up to approximately 2 keV into the first, third and fifth harmonic which is fed into plane or spherical grating monochromator beamlines.^{4–6} At 2 keV the working range of grating monochromators normally ends.⁷ No undulators are operating at BESSY in the x-ray spectral range, because this would require use of superconducting magnet technology. However, since the critical photon energy of the BESSY bending magnets is 2.5 keV, dipole radiation is usable to at least five times that energy. In this “classical” crystal monochromator range the microfocussing x-ray absorption spectroscopy (μ XAS) and microfocussing x-ray diffraction (μ XRD) beamline KMC-2 employing Si–Ge gradient crystals operates between 5 and 15 keV.⁸ High flux hard x-ray radiation is supplied by a superconducting 13-pole wiggler for the magnetic scattering (MagS) beamline,⁹ and by two superconducting wavelength shifters operating the BAMline for material science,¹⁰ the μ -focus beamline for μ XAS and μ XRD,¹¹ and two protein crystallography (PX) beamlines,¹² all of which operate above 5 keV. The 32-pole undulator U125 operated in wiggler mode ($E_c=2.6$ keV) delivers a similar energy spectrum as the bending magnets which is fed into a double crystal monochromator (DCM)

beamline for *in situ* investigation of molecular beam epitaxy (MBE) materials.¹³

This article describes the setup and performance of the double crystal monochromator beamline KMC-1 which was originally transferred from the BESSY I storage ring¹⁴ and which is coupled now to a BESSY II bending magnet port. Its main emphasis is on the *soft* x-ray range to overlap not only with the working range of the VUV grating monochromator beamlines, but also with the BESSY-owned hard x-ray beamlines KMC-2 and μ -focus.

The range between 1.7 and 5 keV is not covered by many crystal monochromators throughout the world, because this requires ultrahigh vacuum (UHV)—surrounding up to—and including the experiment without any vacuum windows which would absorb too much of the radiation. The high energy limit of the beamline at approximately 12 keV is given by the dipole radiation curve. No attempt, however, has been made to cover even lower photon energies (such as 1.5 keV for the Al k edge or 1.2 keV for the Mg k edge), because (1) this range is covered at BESSY sufficiently well by grating monochromators^{4,5} and (2) it would require use of radiation sensitive crystals such as quartz and beryl which combine a low heat conductivity and a high thermal expansion with narrow rocking curve widths.⁴ An alternative for this range, the YB₆₆ crystal, is supposed to be a reasonably radiation tolerant crystal,^{15,16} however, there may be an issue of obtaining these crystals of sufficiently big size to be usable on a bending magnet beamline.

Thus, the low critical energy of BESSY II with its con-

TABLE I. Source characteristics of the BESSY II bending magnets.

Electron energy	1.7 GeV
Magnetic field	1.3 T
Bending radius	4.35 m
Power ($0.3 \text{ A}, 6 \times 0.5 \text{ mrad}^2$)	45 W
Critical energy	2.5 keV
Source size (σ_x)	0.065 mm
Source size (σ_y)	0.04 mm
Source divergence ($\sigma_{y'}$)	$21 \mu\text{rad}$

comitant low thermal load (14 W/mrad at 500 mA ring current) and a useful photon flux up to 12 keV has made possible a simple design of a double crystal monochromator beamline which delivers high flux at crystal limited resolution in a well-focused and stable light spot on the sample.

The multipurpose beamline is in use for a variety of user facilities such as extended x-ray absorption fine structure (EXAFS), near edge x-ray adsorption fine structure (NEXAFS), absorption and fluorescence spectroscopy (XAS). In addition, this beamline is now extensively used for the rapidly developing field of photoelectron spectroscopy at high kinetic energies [HIKE,¹⁷ hard x-ray photoelectron spectroscopy (HAXPES) or volume photoemission^{18–21} (VOLPE)].

II. THE BEAMLINE

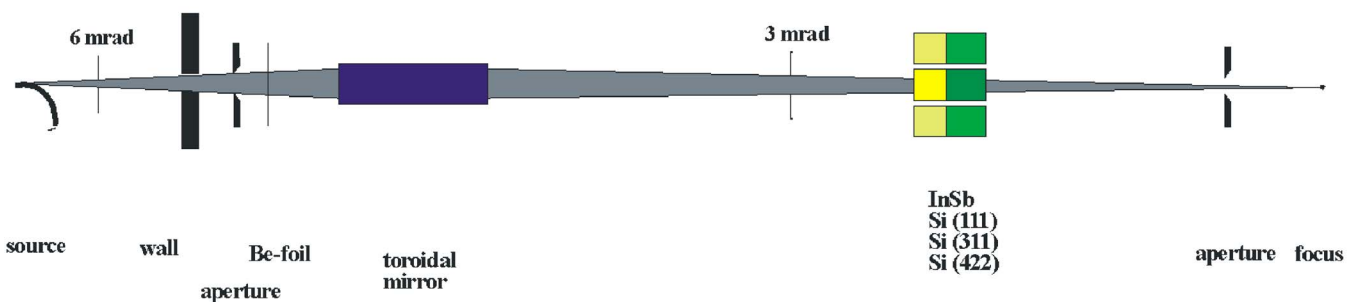
The KMC-1 beamline was set up at the BESSY II port section DIP 1.1B. The beamline was intensively simulated

by ray tracing with the program RAY.²² Source parameters are given in Table I and Fig. 1 shows the schematic setup of the beamline.

The design is governed by the aim to focus as many monochromatic photons as possible with a high energy resolution onto the sample. This requires to have a collimating mirror as close as possible to the source point. Further constraints were the available mirror size of 80 cm and the length of the front end which determines the minimum distance of 13 m from the electron beam source, just outside the radiation wall. In order to avoid too many reflection losses, this premirror is toroidally shaped to focus the beam to the experiment. Thus, a second refocusing mirror is unnecessary in our case. The mirror images the source point into a focus of approximately 0.3 by 0.5 mm^2 which is well matched to many spectroscopy experiments. The DCM is equipped with three pairs of *in situ* exchangeable crystals: InSb, Si (111), and Si (422). The demand for accessing the Si *k* edge at 1.7 keV requires a Bragg angle of as much as 82° .

To reduce the vertical beam divergence—for a better resolving power of the crystal—the mirror focuses the beam in a 1:1.6 demagnification at a focal position of 35.3 m away from the source. In this way the divergence of the incident beam can be reduced to better match the crystal angular acceptance (see Fig. 2), so that at low photon energies (in quasi-backscattering geometry) crystal limited resolution is achievable.

top view



side view

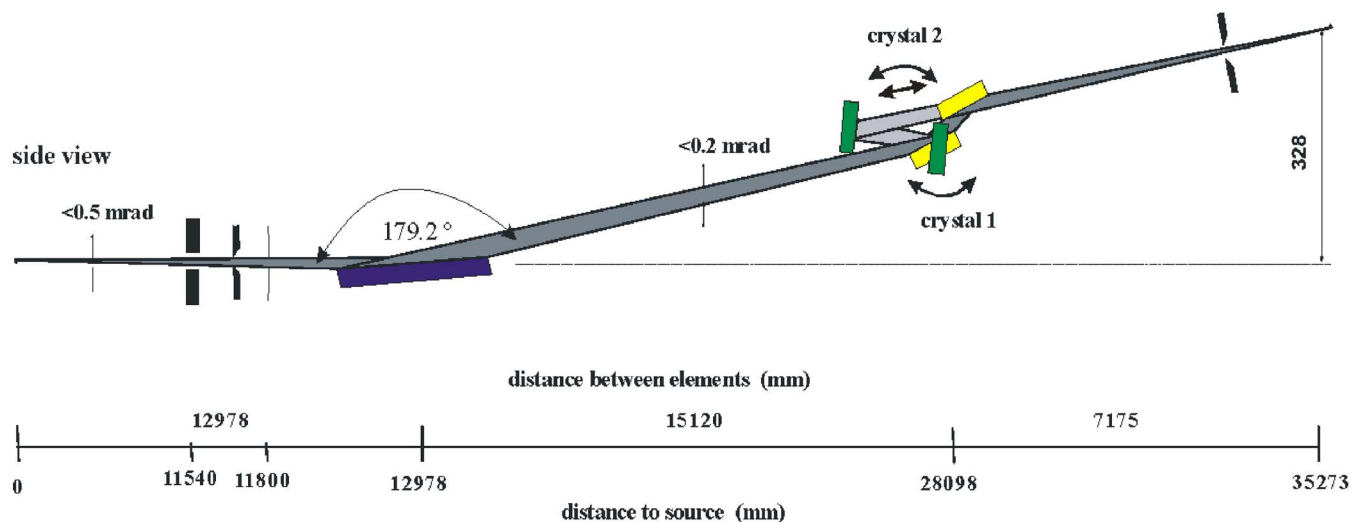


FIG. 1. (Color online) Bending magnet KMC-1 double crystal monochromator beamline with high resolution (crystal backscattering) option. [Si (311) is not installed permanently.]

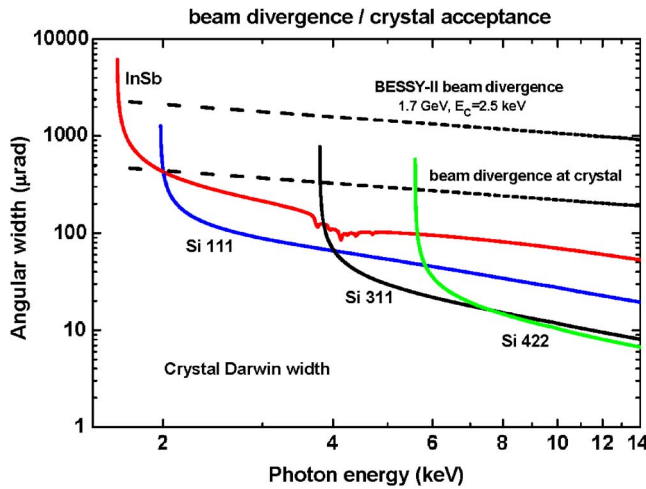


FIG. 2. (Color online) BESSY II vertical beam divergence (with and without premirror collimation) and crystal acceptances for InSb, Si (111), Si (311), and Si (422) orientations. At low energies the Darwin width exceeds the beam divergence and therefore crystal limited resolution is possible here. The kinks in the InSb curve around 4 keV are due to the L -absorption edges of In and Sb,

An Io section in front of the focus spot gives a variety of quick performance checks, diagnostic tools, and beam steering and monitoring possibilities as discussed in Sec II C.

The focus of approximately 0.5 mm^2 size and $3 \times 0.2 \text{ mrad}^2$ in divergence (horizontal \times vertical) is located at a distance of 7.3 m behind the DCM at a height of 1528 mm above floor. It is outside the beamline, 310 mm behind the last valve, to be positioned at the sample position inside the users experimental chamber.

Since the focus position should not move on the sample by less than a small fraction of the spot size, the angular motions of the two crystals must be accurate to better than 1 arc sec. This is accomplished by a variety of measures as described in Sec. II B.

A. The focussing mirror

The mirror parameters are listed in Table II. The toroidal mirror has an acceptance of 6 mrad horizontally and 0.5 mrad vertically. It is made of Si with a 60 nm Pt coating and is operated at 0.4° incidence angle which gives a cutoff energy of 12 keV which coincides with the BESSY II dipole spectrum and the Pt L -absorption edges. Thus, there is no

TABLE II. Mirror parameters.

Optical surface size	800 \times 130 mm
Material	Si/60 nm Pt
Roughness	0.3 nm rms
Mirror parameters	$R=2.35 \text{ km}$ $\rho=115 \text{ mm}$
Acceptance (horizontal \times vertical)	6 \times 0.5 mrad ²
Angle of incidence	0.4°
Distance to the source	12.978 mm
Distance to the focus	22.295 mm
Meridional slope error	<5 arc second
Sagittal slope error	<1 arc second
Maximum absorbed power load	10 W@300 mA

function of this mirror for high order rejection and significant heat load reduction. Heat load is taken away by a water-cooled 100 μm Be foil in front of the mirror. This visible/ultraviolet (VIS/UV) filter reduces the incident power on the—uncooled—mirror surface to less than 25 W (at maximum ring currents of 300 mA) which is mostly reflected to the first crystal.

B. The DCM

At 15 m downstream of the mirror an $(n, -n)$ double crystal monochromator reflects the convergent light beam upwards to the focal position. The Oxford-Danfysik DCM is equipped with three pairs of crystals of 40 by 20 mm² size, of which the first crystal is water cooled: InSb, Si (111), and the high resolution crystal Si (422). They are attached with gallium to a common water-cooled (only the first crystal) Cu-base plate which is connected to a linear translation stage and can be changed *in situ* within a couple of minutes. The minimum photon energy requires a Bragg angle of 82° . For alignment purposes the minimum Bragg angle is -2° degrees and the first crystal can be moved out of the beam to set the optical path free. Energy scanning is done by a rotation of both crystals around the Bragg angle on a large goniometer table, and simultaneous translation of the second crystal parallel ($T1$) and perpendicular ($T2$) with respect to the first crystal's surface to keep the outgoing beam constant both in angle and position and parallel to the incident beam according to

$$T1 = D/(2 \sin \theta), \quad (1)$$

$$T2 = D/(2 \cos \theta). \quad (2)$$

The vertical displacement D between the incident and outgoing beam is set to 25 mm, but it can be changed between 5 and 50 mm at the price of energy tunability.

For positioning of the two crystals, the DCM has six motors, one outside vacuum for the large goniometer table for a parallel rotation of both crystals, and five motors are in-vacuum stepper motors for the translation of the two crystals [first and second crystal change, first and second ($T2$) crystal height, second crystal displacement ($T1$)]. The positioning accuracy is 0.18 arc sec and 1.5 μm . For coarse and fine tuning of the second crystal's pitch and both crystal's roll, three picomotors and three piezotransducers in combination with a positional readout are incorporated, i.e., 15 positional devices all of which are controlled via personal computer (PC) under OS2 using the BESSY-standard AT-bus system. By the piezodevices, the Bragg angle is controlled within the subarcsecond range and settable with a frequency of up to 50 Hz. Table III lists the main technical parameters of the DCM.

C. Io section

A schematic scheme of the diagnostic tools at the end of the beamline is shown in Fig. 3. They are explained in the order of appearance.

TABLE III. DCM parameters.

Bragg angular range	5°–82°
Energy range InSb (111) ($2d=0.748$ nm)	1.674–12.000 eV
Energy range Si (111) (0.627 nm)	1.997–12.000 eV
Energy range Si (422) (0.222 nm)	5.639–12.000 eV
Translational range (T_1)	143 mm
Translational range (T_2)	76 mm
Rotation range—coarse tuning (first crystal roll and second crystal roll and pitch)	0.2°
Rotation range—fine tuning (first crystal roll and second crystal roll and pitch)	60 arc sec
Maximum power on first crystal	15 W at 300 mA

1. Filters

The filters can be inserted into the light path as high- or low-pass filters for selective removal of higher orders or for energy calibration purposes. Thickness is between 1 and 5 μm .

2. Fluorescence screen with pinholes

The screen can be monitored by a TV camera for online-optical control of the beam shape and position. Different aperture sizes between 0.1 and 2 mm vertical with a shape according to the expected beam profile allow for beam shaping.

3. Pinholes

To define the beam size and position between 0.14 and 2.5 mm.

TABLE IV. Back reflection photodiodes (Ref. 23 and 24).

Back reflection	Photon energy (eV)	Intrinsic resolution (eV)
Si (111)	1978.2	0.20
Si (333)	5931.2	0.052
Si (444)	7908.3	0.04
Si (555)	9885.3	0.015
Si (400)	4566.1	0.110
Si (800)	1978.2	0.027

4. Backscattering photodiodes

Si (nm) and Si (n00) photodiodes (Silicon Sensor) mounted perpendicular to the beam (Bragg angle of 90°) to be used for energy calibration and energy resolution tests. At this angle the resolving power is crystal limited and, therefore, at the corresponding photon energies, the rocking curve width measured in absorption directly yields the resolving power of the incident beam.^{23,24} Table IV lists the various Bragg reflections available.

5. Io monitors

The photoelectric yields on a Au or Cu mesh (80% transmission), which is in the picoampere range, can be used as Io signal during data taking.

6. Flux monitors

For absolute determination of the photon flux, an Au photocathode and a Si (AXUV-100) or GaAsP photodiode of different sizes can be inserted into the beam.

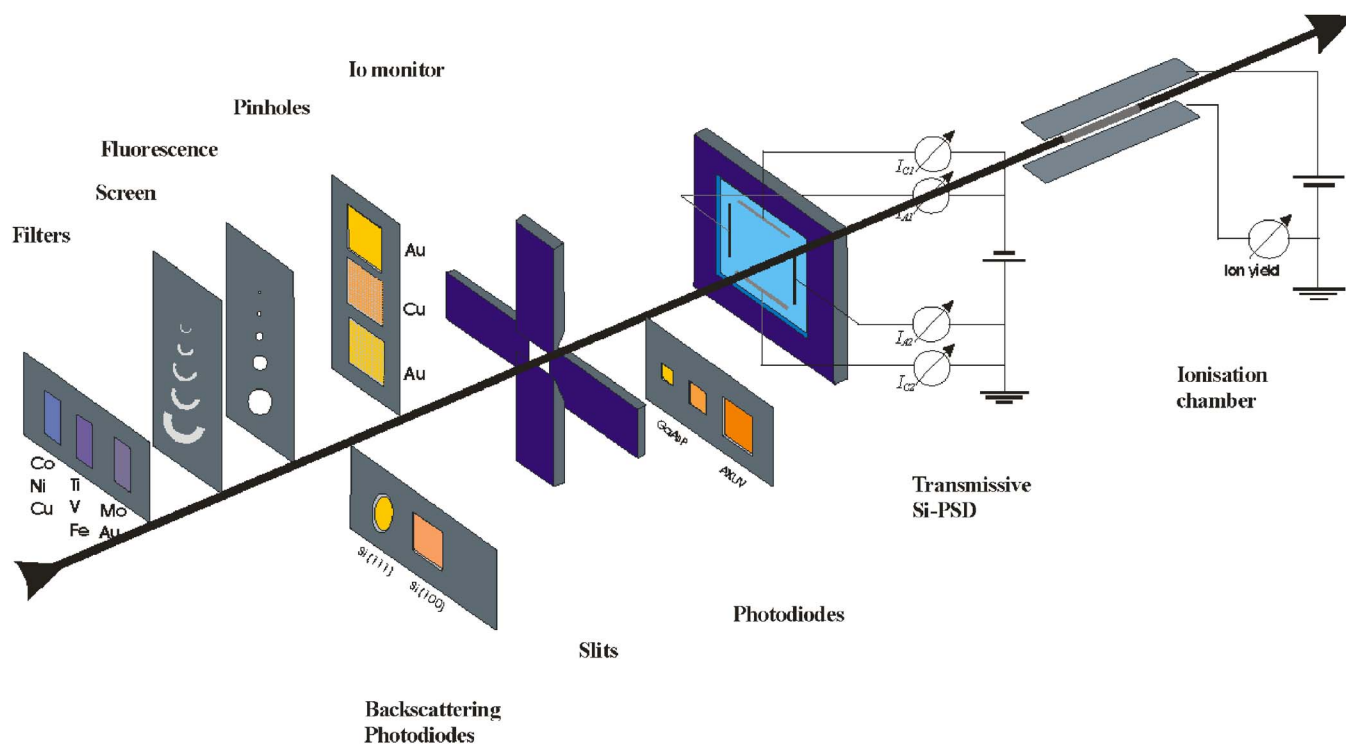


FIG. 3. (Color online) Diagnostic and beam shaping and monitoring tools in the Io section.

7. Variable slits

Horizontal and vertical slits allow for positioning and shaping of the beam.

8. Ionization chamber

The ionization chamber signal (typically in the nanoampere range) is the standard Io signal. This signal is used as input for the monochromator stabilization (MOSTAB) feedback control of the second crystals's pitch for continuous control of the rocking curve intensity at its maximum, or at a certain fraction of it for high order removal (see Sec. III D).

9. Transmissive Si PSD

A newly developed two-dimensional position-sensitive diode (2D PSD) on the basis of a Si photodiode, thinned down to 3 μm thickness, gives a position signal in both horizontal and vertical directions with a 1 μm resolution. This device allows for the first time a feedback in both directions to stabilize the beam on the sample (see Sec. III E).

III. PERFORMANCE

After an extensive commissioning period, the KMC-1 beamline is in continuous operation since summer of 2004 and it is widely used for a variety of experiments on, e.g., fluorescence absorption and photoelectron spectroscopy as well as for high-precision reflectometry. Some examples will be shown in the next section. In this section the results of the beamline commissioning are presented.

A. Photon flux

According to Sec. II C there are a variety of diagnostic tools at the end of the beamline, which make a quick *in situ* characterization and long-term tracing of the performance possible. The intensity measurements are routinely done with Si or GaAsP photodiodes because of their high efficiency in the x-ray range with photocurrents in the 10^{-5} A range. The flux available at the experiment is shown in Fig. 4 for all three crystals InSb, Si (111), and Si (422). The flux data were calculated according to the GaAsP efficiency.²⁵

For typical BESSY II ring currents of up to 300 mA, the photon flux is in the 10^{11} – 10^{12} photons/s range throughout the whole available energy range. The Si (422) has an order of magnitude less flux, but higher energy resolution. The flux at low energies is going down by the finite transmission of the 100 μm Be foil, while the high energy cutoff is determined by the *L* edges of the Pt-coated mirror and by the BESSY II dipole spectrum ($E_c = 2.5$ keV). The Si (111) spectrum has been measured within one scan using the MOSTAB feedback control. Around 4 keV the InSb is hardly usable due to absorption at the In and Sb *L* edges. Due to the peculiar beamline design, these flux data are comparable—if not superior—to the flux obtained at the BESSY II wavelength shifter beamlines^{10,12,13} because (1) this beamline collects an unusually large fraction of the horizontal fan of 6 mrad and (2) the WLS spectrum dominates at higher energies ($E_c > 10$ keV).

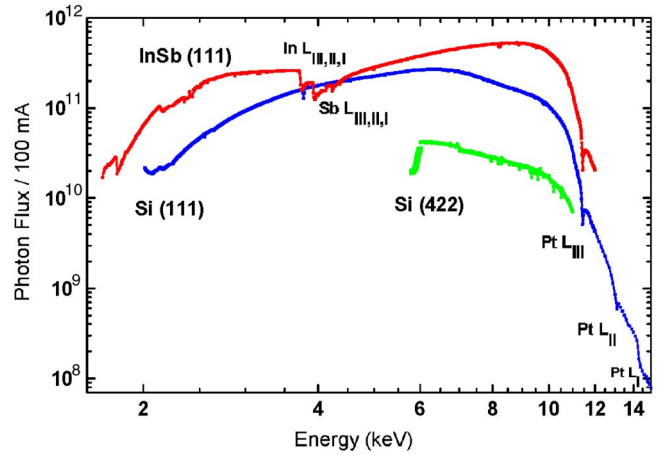


FIG. 4. (Color online) Photon flux of the InSb, Si (111), and Si (422) crystals determined with a GaAsP photodiode.

B. Energy resolution

According to the Bragg equation the lowest photon energy requires a maximum Bragg angle of as much as 82° . This is nearly normal incidence or close to backscattering geometry. At these large Bragg angles—which are unusual for synchrotron radiation-crystal monochromators—crystal optics behaves differently from standard grazing-incidence optics, and, especially, the behavior of the resolving power gets very interesting. This “built-in” normal incidence crystal optics (backscattering geometry) is intrinsically coupled to a high energy resolution according to

$$\Delta E = E \Delta \theta / \tan \theta, \quad (3)$$

with θ the Bragg angle and $\Delta \theta$ the rocking curve width.

The rocking curve width,

$$\Delta \theta = \sqrt{((\Delta \theta_{\text{cr}})^2 + \psi^2 + (\varphi^2 \tan^2 \theta / 8)^2)}, \quad (4)$$

is determined by the intrinsic crystal Darwin width $\Delta \theta_{\text{cr}}$ and by the sagittal and meridional beam divergences ψ and φ . Thus, crystal limited resolution is achievable using vertically collimated incident light, with ψ and φ being close to zero. (The influence of the divergence in nondispersive direction φ on the resolution is in general omitted, since it is negligible at the small divergences which are typical for synchrotron radiation.²⁶) Alternatively, however, at large angles the tangent term is dominating, the beam divergence does not affect the resolution significantly, and crystal limited resolution is also possible, more or less regardless of the beam divergence (see also Fig. 2).

To determine the energy resolution, different methods were applied. In Fig. 5 the photoabsorption measurements are shown using a Si (*nnn*) photodiode in normal incidence to the incident beam (see Sec. II C 4). According to Eq. (3) the resolving power in normal incidence ($\theta = 90^\circ$) is crystal limited, so that the total resolving power is determined primarily by that of the incident light. The Bragg-absorption minimum is therefore a direct measure of the resolving power of the incident beam. So, the Si (422) crystal has an full width at half maximum (FWHM) energy resolution of

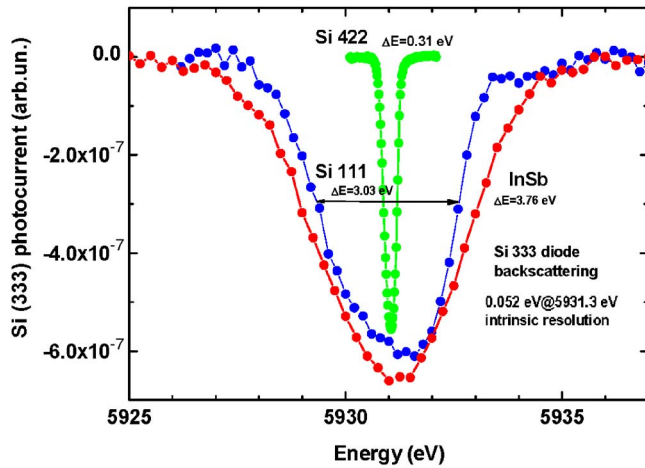


FIG. 5. (Color online) Energy resolution of all monochromator crystals determined by Bragg reflection on a Si (333) photodiode in normal incidence at 5931.3 eV.

0.31 eV at 5931.3 eV, while that of Si (111) crystal is ten times larger which coincides with the flux ratio of 10 between both crystals.

A second independent method for the determination of the beamline resolution, namely, photoelectron spectroscopy (PES) has been used. The technique of PES at high kinetic energies (HIKE) is explained in Sec. IV B. PES has the advantage that these data can be obtained continuously, at each photon energy; however, the spectra have to be fitted adequately with a complicated profile to disentangle the contributions of beamline and spectrometer instrumental resolution as well as the core hole lifetime broadening. The PES data have the further advantage that the electron spectrometer is an energy-dispersive detector and therefore it is able to separate the higher diffraction orders in the incident beam.

The third and fourth order excitation energies can be used *simultaneously* within a HIKE spectrum, such that, in principle, an *in situ* depth profiling of a sample—*within* one scan—is possible. This is demonstrated in Fig. 6, where the

TABLE V. Fitted resolution data for the Au $4f_{7/2}$ data of Fig. 6.

	First order Si (111)	Third order Si (333)	Fourth order Si (444)
Photon energy (eV)	2002	6006	8008
Acquisition time (min)	4	40	180
Lorentzian FWHM (eV)	0.348	0.348	0.348
Gaussian FWHM (eV)	0.243	0.135	0.185
Analyzer resolution (eV)	0.125–0.140	0.125–0.140	0.125–0.140
Beamline resolution (eV)	0.21 ± 0.01	0.050 ± 0.02	0.073 ± 0.02

Au $4f$ lines have been measured at 2002, 6006, and 8008 eV in the first third, and fourth diffraction orders of the Si (111) crystal. Beamline optimization for higher order intensity requires a slight detuning of the monochromator crystals. Taking into account that, not only the flux in higher crystal orders, but also the cross section decreases dramatically with higher kinetic energy, the acquisition of typical high resolution low-noise HIKE spectra such as Au $4f$ takes between 1 min (Si (111)) and some hours [employing Si (333) or (444)]. The Au $4f_{7/2}$ line was fitted by a Doniach-Sunjic profile²⁷ which is a convolution of two functions, a Lorentzian and Gaussian—includes an asymmetry parameter. The Lorentzian function estimates the lifetime (0.348 eV) and the Gaussian and function stands for the instrumental broadening given by the spectrometer and beamline.²⁸ These data are given in Table V.

In Fig. 7 all energy resolution data extracted either from crystal-optical measurements or from the HIKE Au photoemission are shown. The tangential behavior of the resolution according to Eq. (1) is clearly seen for all crystals. At low energies, the resolution is crystal limited—despite of the divergent SR beam. At 2 keV, the Si (111) has a resolution of 200 meV. At 6 keV, a beamline resolution of 50 meV (± 20 meV) using Si (111) in third order has been measured at standard beam divergence (without any flux-consuming collimation). At 8 keV, the resolution is 70 meV (± 20 meV)

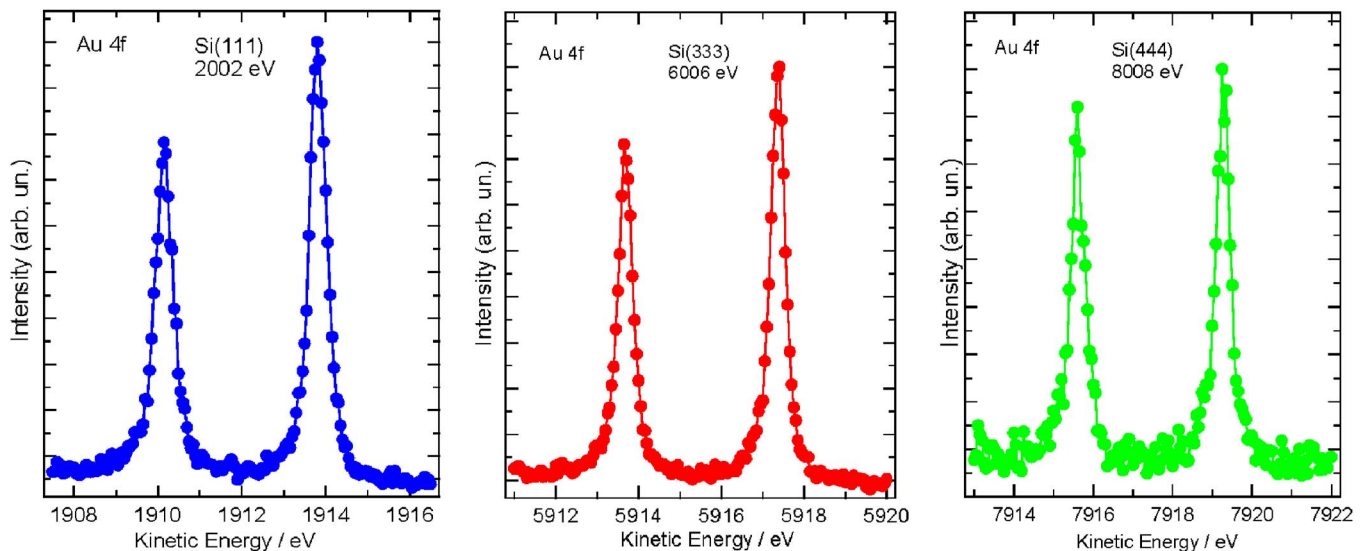


FIG. 6. (Color online) Photoelectron spectra of Au $4f_{5/2}$ and Au $4f_{7/2}$ core levels obtained using the KMC-1 Si (111) crystal tuned to 2002 eV photon energy. Spectrometer pass energy was 100 eV, and entrance slit 0.5 mm.

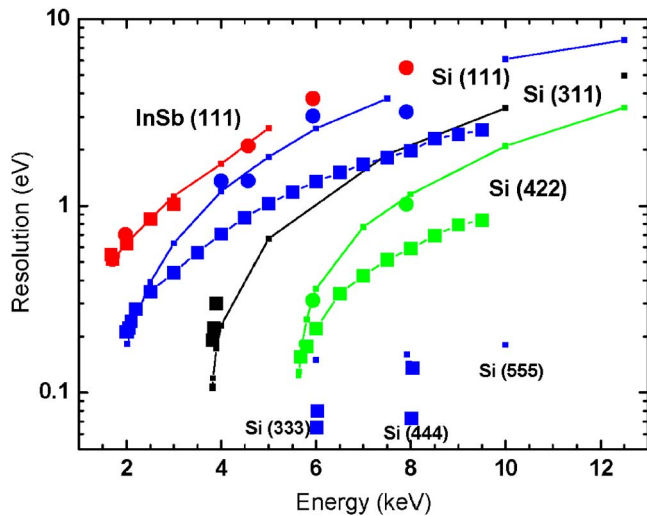


FIG. 7. (Color online) Calculated (small points and lines) and experimentally determined (solid circles, solid squares) resolving power of the KMC-1 monochromator crystals InSb (111), and Si with (111), (311), and (422) orientations. Si (333) and Si (444) correspond to higher order radiation. The solid circles have been measured by the photocurrent absorption drop (FWHM) in a single-crystalline Si photodiode with (nnn) and (400) orientation operated in back reflection (see Fig. 5). [Si (311) is not installed permanently.]

using Si (111) in fourth order. This corresponds to a resolving power $E/\Delta E$ of more than 100,000.

By the use of high crystal reflection orders [Si (333) and (444)] this high resolution option ($\Delta E < 500$ meV) is available nearly *continuously* within the complete spectral range. Ultrahigh resolution ($\Delta E < 200$ meV) is available at selected photon energies (2, 5.7, 6, and 8 keV). Thus, any flux-consuming postmonochromatization employing Si (nnn) channel cut crystals is unnecessary in our case.

C. Spot size

The focal spot was determined by a charge coupled device (CCD) camera which was translatable along the beam to

also determine the beam divergence. The picture is shown in Fig. 8(a). The shape and size are in coincidence with spot patterns obtained by ray tracing [Fig. 8(b)] and it is basically due to the aberrations of the toroidal mirror used for focusing, while source size and slope errors play a minor role on the imaging quality. The FWHM size is 0.38×0.66 mm² (horizontal \times vertical). The divergence was measured to be 3×0.2 mrad² (horizontal \times vertical). No attempt has been made so far to further reduce the focus size by a secondary focus stage such as capillary optics.

D. High orders

For some experiments, high diffraction orders in the incident beam may be disastrous; for some other, they may be advantageous. One such experiment of the last kind has been shown in Sec. III B which benefits from the good resolving power achievable. The demands for the beamline operation thus vary between optimum elimination of higher orders and flux optimization into a certain high order.

High diffraction orders of the Si (111) monochromator crystal were measured by an energy-dispersive Ge(Li) detector. Because of the low BESSY II critical energy of 2.5 keV, the higher orders have a significant contribution in the beam only at the low energy side of the working range. The premirror does not act at all as a high order filter. The worst case situation is shown in Fig. 9. Here, the spectrum is shown for the Si (111) crystal set close to its low energy limit of 2000 eV. Up to the eighth order can be identified. Note that the second order is a “forbidden” reflection in the (111) plane of cubic Si crystal. Nevertheless, there seems to be significant nonzero (222) diffracted intensity, due to the atomic bond orbitals and to anharmonic vibrations.

The third order can be as much as 35% of the first order, while the fourth order contributes 6%. The data, however, have not been normalized to the detector efficiency. This large high order fraction is due to the fact that the first order is strongly suppressed by the 100 μ m Be foil which absorbs

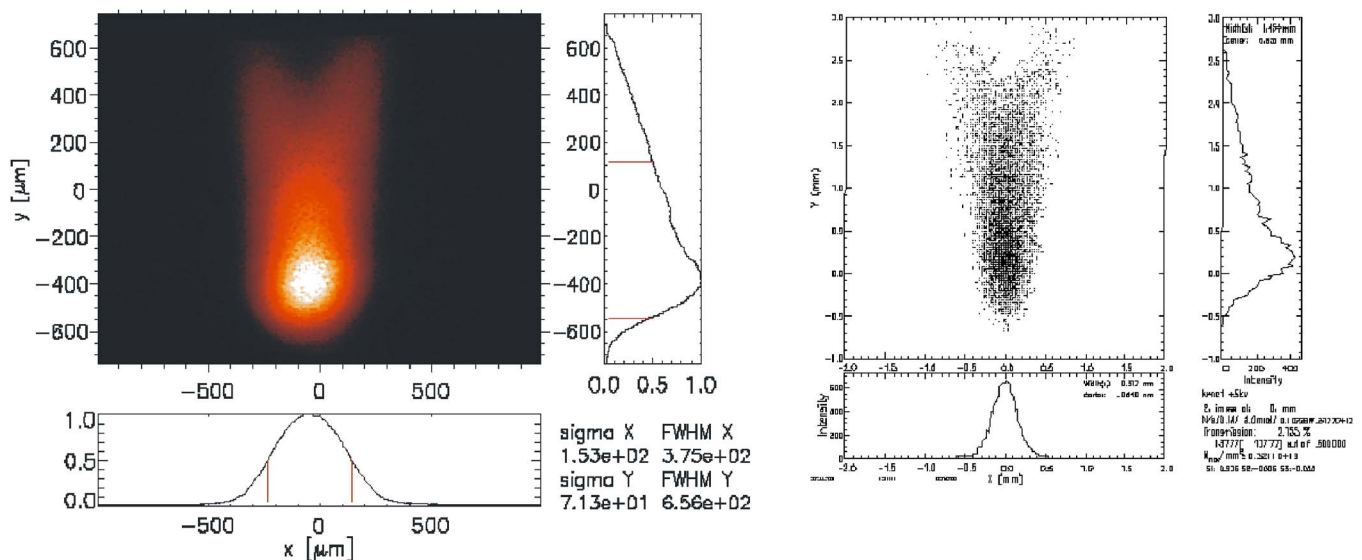


FIG. 8. (Color online) Real (a) and ray tracing (b) image of the BESSY II electron beam 35 m downstream the KMC-1 beamline. The FWHM focus size is 0.38×0.66 mm², the beam divergence is 3×0.2 mrad² (horizontal \times vertical).

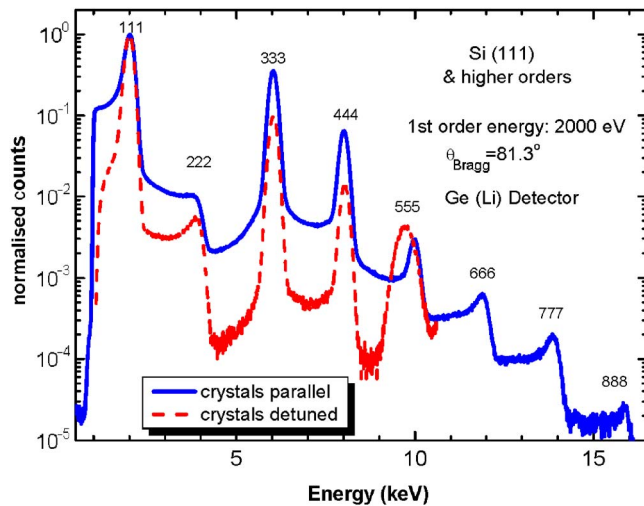


FIG. 9. (Color online) Higher order crystal reflections of Si (111) at a photon energy setting of 2000 eV for a parallel setting of both crystals (full curve), and for the detuning case (dotted curve). Note that the second order reflection is forbidden. Spectra were obtained with an energy-dispersive Ge(Li) detector. The data are not normalized to the detector efficiency.

75% of the 2000 eV radiation. When the crystals are detuned slightly the higher orders can be significantly reduced down to less than 10% (1% for the fourth order). Thus, the higher order flux contribution can be significantly influenced by the relative angular setting of the crystals, since the rocking curve widths are different and the rocking curve centers may be slightly displaced with respect to each other due to thermal effects which are negligible in the first order. This is confirmed by the data of Fig. 10. Here, the flux values calculated by systematic ray tracings are shown for the first, third, and fourth orders Si (nmn) at a first order energy of

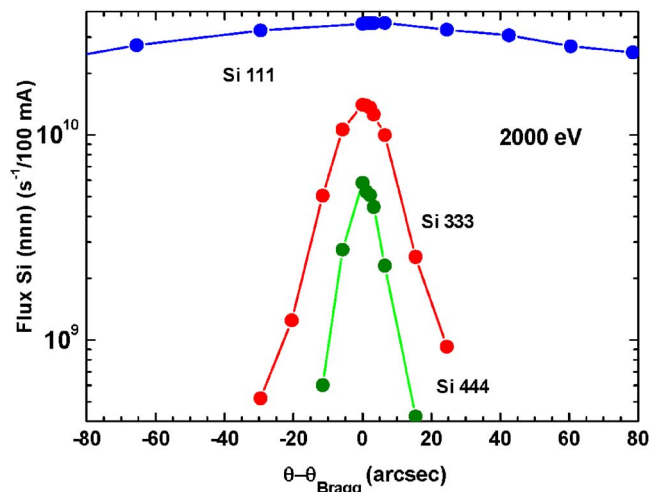


FIG. 10. (Color online) Calculated photon flux at the Si (nmn) high order crystal reflections for a photon energy setting of 2000 eV as function of the crystal's detuning angle.

2000 eV. Thus, high orders can be suppressed from 40% to less than 1% by a crystal offset angle of 30 arc sec.

E. Horizontal beam stability

Contemporary x-ray beamlines based on crystal monochromators require excellent stability of the monochromatic beam. Moving further towards higher brilliance, microfocus, and automated beamline operation, beam monitoring and feedback schemes are crucial. For monitoring, x-ray beam position monitor (XBPM) can provide information about intensity, position, and shape of an x-ray beam along a beamline. While imaging monitors can provide all three parameters at once for beam adjustment, they are inherently limited in time resolution and occlude the beam in most cases. Most center-of-mass-type XBPMs, on the other hand, can provide beam position information at high time resolution, a parameter of central importance for monitors to be used in feedback schemes. *In situ* operating XBPMs (allowing for on-the-fly intensity and position control) while combining large active area at submicron resolution and full feedback capability are of great importance.

Such a prototype *in situ* detector based on a transmissive silicon-PSD detector thinned down to approximately $3 \mu\text{m}$ is now in routine use in the beamline. It has been developed within a joint project initiated at BESSY (Ref. 29) and shared by a semiconductor manufacturer.³⁰ First results obtained on the KMC-1 beamline have been shown in Ref. 31. Figure 11 gives an impression on the horizontal beam stability achievable during an energy scan.

The piezoactuator voltage for the roll movement of the second crystal of the double crystal monochromator was controlled in a proportional-integral-derivative (PID)-feedback loop to minimize the position signal (difference/sum) and, thus, to lock the beam to the center of the PSD detector 6.5 m downstream [see Fig. 11(a)]. While the photon flux within the monochromatic beam is regulated by a MOSTAB-controlled intensity feedback on the ionization chamber signal [Fig. 11(c)], a correction scheme based on the new PSD detector was employed here to fight the beam motion at low energies. In Fig. 12(b) the cases with feedback on and feedback off are compared demonstrating that the feedback loop detects and locks the beam drift, which corresponds to a motion of 0.6 mm off the detector center when the feedback is switched off.

The horizontal travel of the beam is determined by the mechanical accuracy of the translation stage of the DCM assembly. For beam stability, the low energy end resembles the worst case: the change of the Bragg angle per energy is largest here ($0.1^\circ/\text{eV}$). Thus, a short energy change of 100 eV requires a Bragg angle change from 70° to 80° and a translation $T_2=32$ mm of the second crystal. This translation produces a residual horizontal angular deviation of 0.18 mrad behind the DCM. At higher energies (i.e., smaller Bragg angles) this problem becomes negligible.

Thus this first detector prototype for the transmissive PSD-XBPMs has already proven its great potential for beam monitoring and for their use in combined position and intensity feedback schemes for crystal monochromator beamlines.

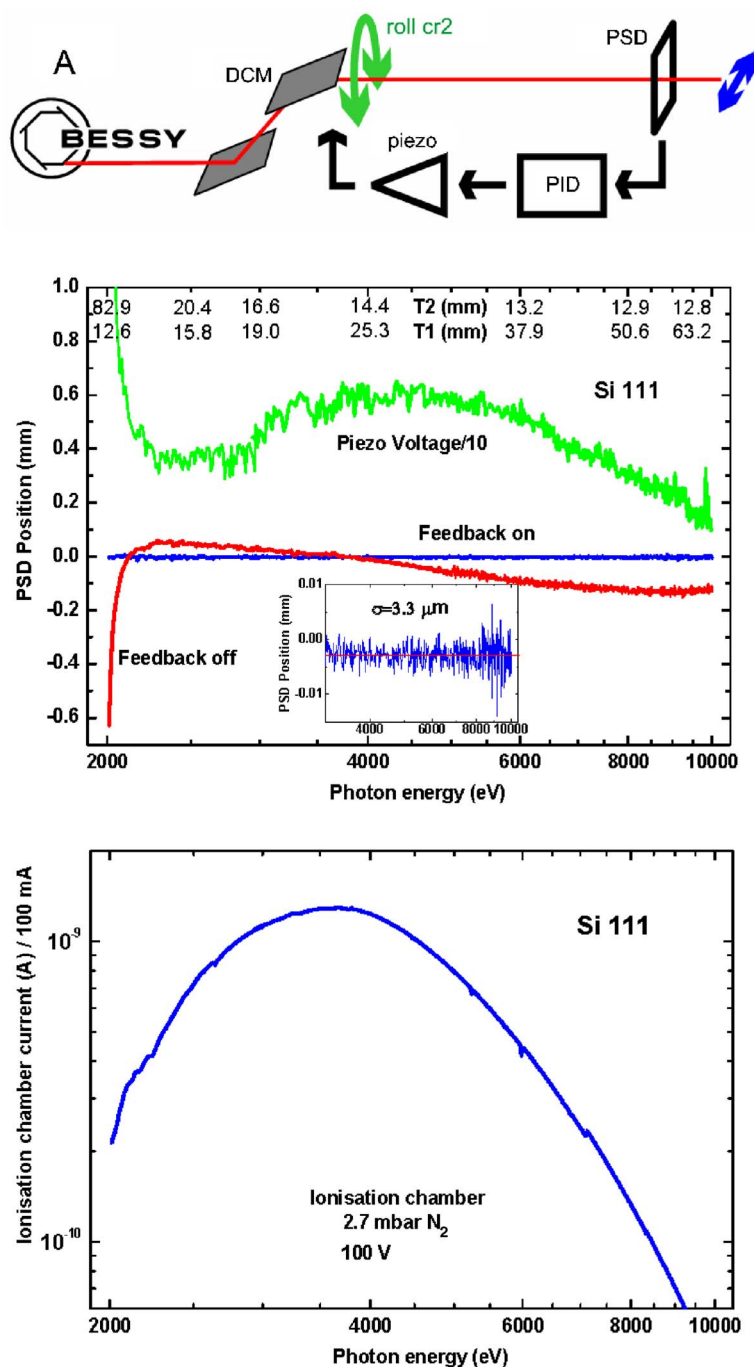


FIG. 11. (Color online) (A) Schematic of the KMC-1 beamline horizontal feedback loop. (B) PSD-position signal for feedback on (blue) and off (red) and piezoactuator voltage (green). (C) Intensity signal after PSD measured with ionization chamber. Horizontal position stability is better than $5 \mu\text{m}$. The nonlinear travel ranges T1 and T2 of the second crystal during energy scan is indicated in (b), top scale.

IV. EXPERIMENTAL RESULTS

A. X-ray absorption spectroscopy

1. BioXAS

XAS has become one of the most important techniques to analyze the nuclear geometry at the atomic level (by EXAFS) and oxidation state (by XANES) of metal centers in biological metalloenzymes during catalysis.^{32–35} At the KMC-1 at BESSY an experiment for XAS on biological samples (BioXAS) has been set up which consists of an energy-resolving single-element Ge detector, a digital signal

processor, and a helium cryostat. XAS measurements are performed on synthetic model compounds and on the metal complexes of metalloenzymes. The KMC-1 beamline is well suited for BioXAS experiments on ultradilute biological samples. The energy range allows for XAS measurements on the most important metals (e.g., Ca, V, Mn, Fe, Ni, Cu, and Zn) in biological and synthetic systems. A typical EXAFS raw data transmission spectrum on a Mn complex is shown in Fig. 12. Energy calibration is routinely done by observing (1) the Mn pre-edge peak (6543.3 eV) and (2) the transmis-

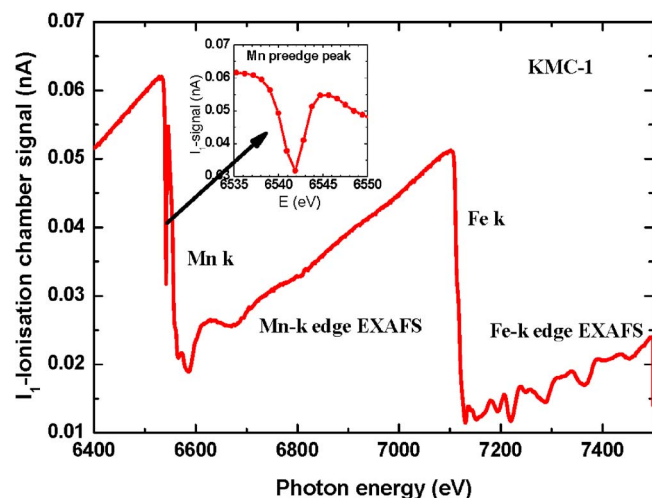


FIG. 12. (Color online) EXAFS obtained in transmission mode on Mn k edge on a diluted Mn sample. The Mn pre-edge peak and an Fe foil as reference in front of the I1 ionization chamber deliver an energy offset of better than 1.5 eV. Energy stability is better than 0.1 eV/day. Measuring time/energy point was 1.6 s, total accumulation time is 31 min.

sion through an Fe foil (Fe k edge at 7112.0 eV) which is in between the sample and the I1 ionization chamber.

One focus of the research is the manganese complex of photosystem II. At this sophisticated tetranuclear metal center, the dioxygen of the atmosphere is produced by the oxidation of water molecules, driven by the energy of sunlight ($2\text{H}_2\text{O} + 4h\nu = \text{O}_2 + 4\text{H}^+ + 4\text{e}^-$).

XAS spectra of the manganese complex of high quality have been obtained both in the XANES and EXAFS regions, and novel information has been derived (Fig. 13). By using XAS on two-dimensionally oriented photosystem II samples, using the polarized x-ray beam to perform linear-dichroism measurements, changes in the oxidation state and the atomic structure of the manganese complex during the four-stepped catalytic cycle of water oxidation and the assembly of the metal center in the light are investigated.^{33,34}

2. Material science

Nanostructured ceramic coatings are being intensively investigated because they open a wide field of new materials with improved mechanical and tribological properties.³⁶⁻³⁸ The final behavior of such coatings depends on their composition and microstructure. Silicon addition in nitride compounds has shown to improve significantly their hardness.^{39,40} For instance, in the Ti-Si-N coating system, coating hardness ranging from 40 to 80 GPa has been reported in the composition range of 2–20 at. % Si. To explain this improvement, a detailed investigation on composition, structure, and atomic short-range order surrounding Ti and Si atoms is needed. XAS is a very appropriate tool for this kind of studies since it is very sensitive to the local environment around a specific atomic element, giving information on the composition, structure, and short-range symmetry.

In this work, several TiSiN and AlCrSiN coating compounds with different Si contents have been studied by XAS

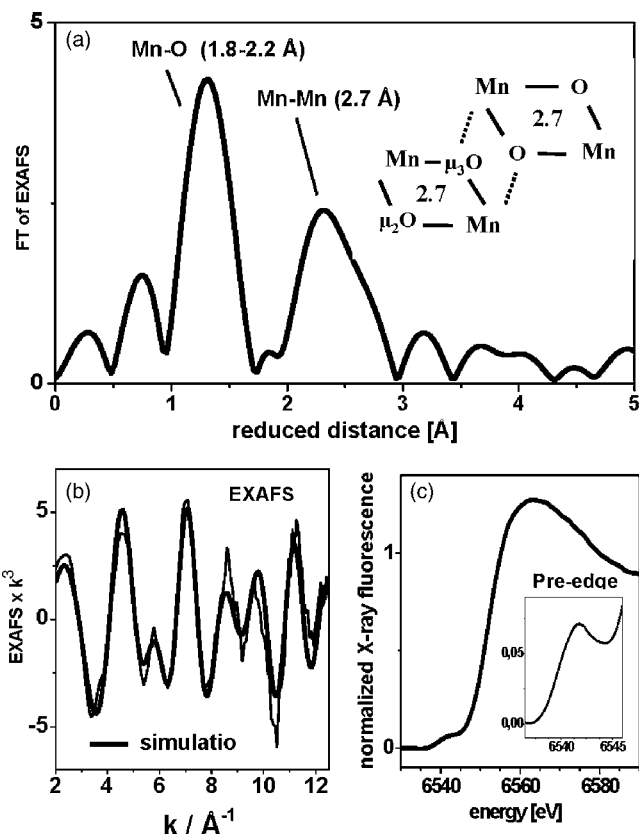


FIG. 13. The oxygen of the atmosphere is produced by water oxidation at the manganese complex of photosystem II of green plants. Distinct structural motifs of the tetranuclear metal center are accessible by x-ray absorption spectroscopy at the Mn K edge. EXAFS analysis [(A) and (B)] provides the interatomic distances (Mn-O and Mn-Mn) with high precision (0.02 Å). The XANES spectrum (C) is indicative of the Mn oxidation state and the local nuclear geometry and electronic structure.

in order to investigate the effects of silicon addition on the composition, structure, and phase development of these coatings. AlCrSiN thin films have been obtained by cathodic arc evaporation, whereas TiSiN coatings have been grown by magnetron sputtering. Changes in the structure and chemistry of the Si-containing coatings as compared with those without Si can influence the mechanical properties, grain size and morphology, defect content, film porosity, or phase content of these films. To get some insight on these changes, x-ray absorption spectra have been measured at the Si, Cr, and Ti K edges in fluorescence yield mode. XAS measurements were carried out using a standard chamber equipped with a solid state fluorescence detector.

Figure 14(a) shows XAS spectra at the Ti K edge of TiSiN samples with different Si contents. In this case, all spectra keep a similar line shape to that of titanium nitride, independently of Si content. The pre-edge region, which is associated to transitions from Ti $1s$ states to Ti $3d$ states hybridized with Si $2p$ states, does not show significant changes with silicon addition. This suggests a weak interaction between Ti and Si.

Figure 14(b) shows XAS spectra at the Si K edge of the same TiSiN samples, as well as a SiO₂ single crystal, as a reference sample for comparison. In all cases the spectral line shape is typical of amorphous Si₃N₄,⁴¹ with a main peak

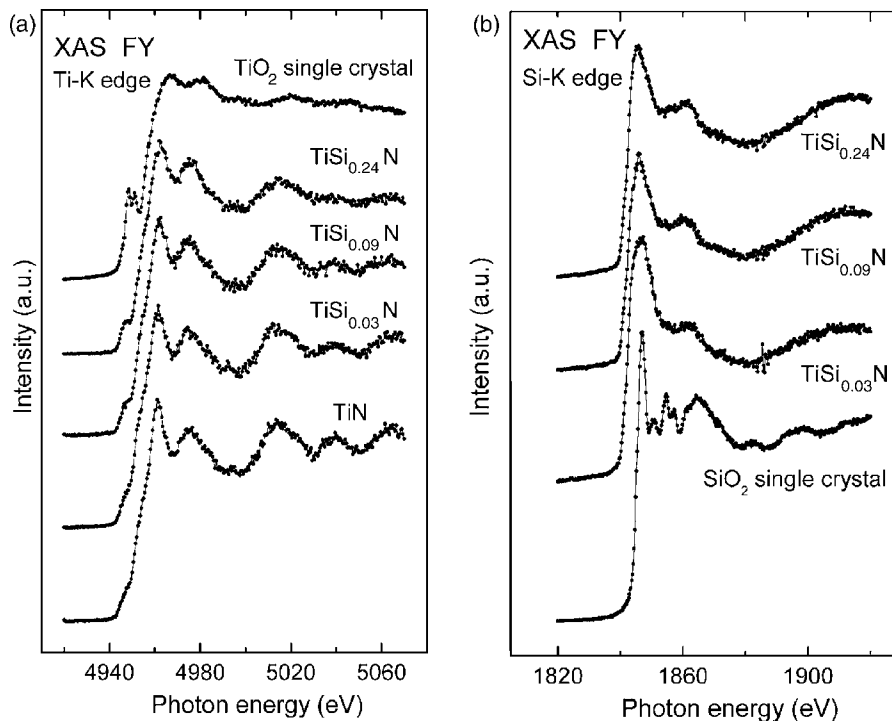


FIG. 14. X-ray absorption spectra in fluorescence yield mode at the Ti *K* edge [Fig. 14(a)] and at the Si *K* edge [Fig. 14(b)] for several TiSiN coatings with different Si contents. Additionally, Si *K*-edge spectra for Si, SiO₂, and *α*-Si₃N₄ are shown for reference.

at 1845 eV and a weaker structure at 1861 eV. The main peak of SiO₂ is located at 1847 eV, so we cannot exclude the presence of SiO₂ for very low Si content. Except for this small oxygen presence, no significant changes in the line shape is observed with silicon content. Hence, both Ti *K* and Si *K* XAS results suggest that the interaction between Ti and Si is weak and that amorphous Si₃N₄ aggregates are formed inside a TiN matrix. In the TiSiN system, we have observed features corresponding to *α*-Si₃N₄ in all of the deposited samples and there was not any significant change with silicon content. Both Ti *K* and Si *K* spectra suggests that there was a weak interaction between Ti and Si.

B. HIKE

Electron spectrometers with highly stabilized high voltage power supplies are available nowadays which have an ultrahigh resolution of not more than 20 meV at kinetic energies up to 15 keV. This high kinetic energy photoemission at hard x rays (HIKE or HAXPES) is an ideal-nondestructive—tool to look deeply into bulk material (>5 nm) and to study (buried) interface layers.^{42,43} For this technique hard x rays with similar resolving powers at highest flux are required.

The KMC-1 beamline has been used in the last years to successfully establish this HIKE technique employing a Gammadata Scienta R-4000 hemispherical analyzer¹⁷ optimized for high kinetic energy electrons up to 10 keV. Despite of the low photoelectron cross sections at high excitation energies, core levels of multilayer interfaces and “real” solar cell samples at probing depths of more than 10 nm could be investigated.⁴⁴

In Fig. 15 HIKE overview spectra of a Cu(In,Ga)Se₂ (CIGS) film with Zn (O,S) buffer layer obtained in the energy range of 3000–9000 eV are shown.⁴⁵ The spectra allow

for an in-depth scan of the device structure to be made. In particular, the successive appearance of the CIGS film signals (Se 2*p*, Cu 2*p*, and Ga 2*p*) with increasing photon energy through the 15 nm thick buffer layer can be nicely monitored. These results open up completely new possibilities for the study of properties of real devices of this type, relating structural and electronic properties to device performance.

Figure shows HIKE spectra of a chalcopyrite thin film solar cell device obtained at an energy of 4000 eV.^{46,47} Here, the Cu depletion towards the chalcopyrite surface which is crucial for the solar cell efficiency was investigated. The Cu diffusion upon *in situ* heating was investigated for different In₂S₃ buffer layers deposited by various processes on chalcopyrite absorbers. In Fig. 16 the evolution of the Cu 2*p* core level with heating temperature was followed. The copper has diffused into the indium sulfide already at low temperatures, the surprising fact is that the copper content remains constant under additional heating until 270 °C when it begins to rise again. This corresponds well to the temperature at which the solar cell performance begins to degrade and, therefore, it is postulated that the In₂S₃ structure which contains copper, transforms into a CuIn₅S₈ phase and the abrupt change in copper composition would appear to agree with a phase change. An excitation energy of 4000 eV allows a significant fraction of the 20 nm thick layer to be examined and thus, the experiment is not considered to be surface specific as in the case of conventional x-ray photoemission spectroscopy (XPS). These results open up completely new possibilities for the study of properties of real devices of this type, to determine, e.g., depth dependent element ratios relating structural and electronic properties to the device performance.

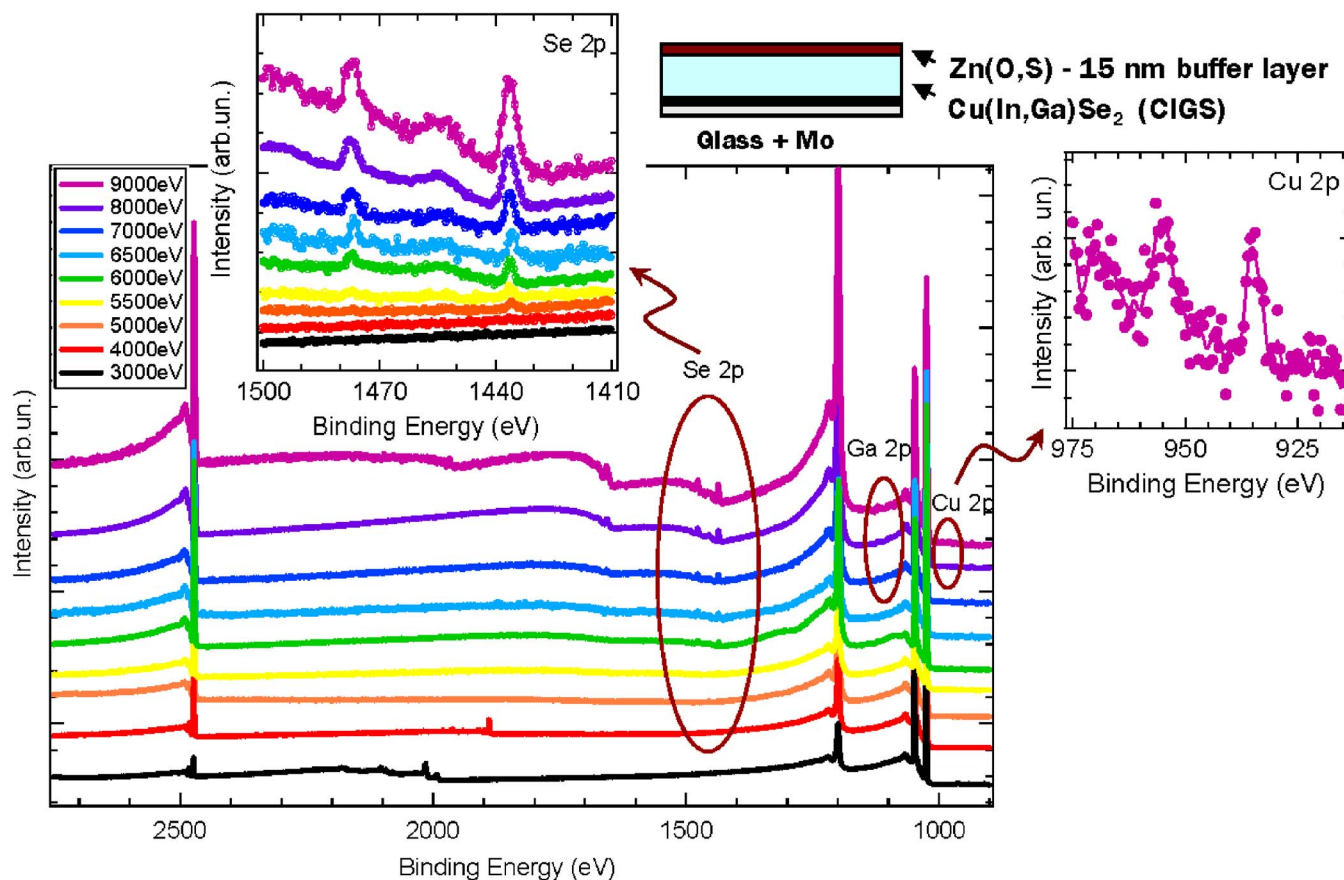


FIG. 15. (Color online) HIKE overview spectra obtained at photon energies 3000–9000 eV (bottom to top curves) from a CIGS film with 15 nm Zn(O, S) buffer overlayer (Ref. 45).

V. CONCLUSION

The BESSY bending magnet beamline KMC-1 has been successfully set up and has proven in the last years to be very versatile to meet different experimental requirements such XAS, fluorescence spectroscopy, reflectometry, and photoelectron spectroscopy at high kinetic energies (HIKE). Despite of the low photoelectron cross sections at high excitation energies, core levels of multilayer interfaces and “real” solar cell samples at probing depths of more than 10 nm could be investigated.

The reason for the good matching of this beamline to different experimental requirements is basically due to the facts that this beamline not only has a high flux (10^{11} – 10^{12} photons/s) in a 500 μm focus size, which is well matched to the sample or detector/spectrometer acceptance, and a continuously tunable working range between 1.7 and 12 keV, so that many biologically or technologically important k -absorption edges can be addressed, but also and most importantly—a very good energy resolution. All this could be achieved by (1) the windowless setup under ultrahigh-

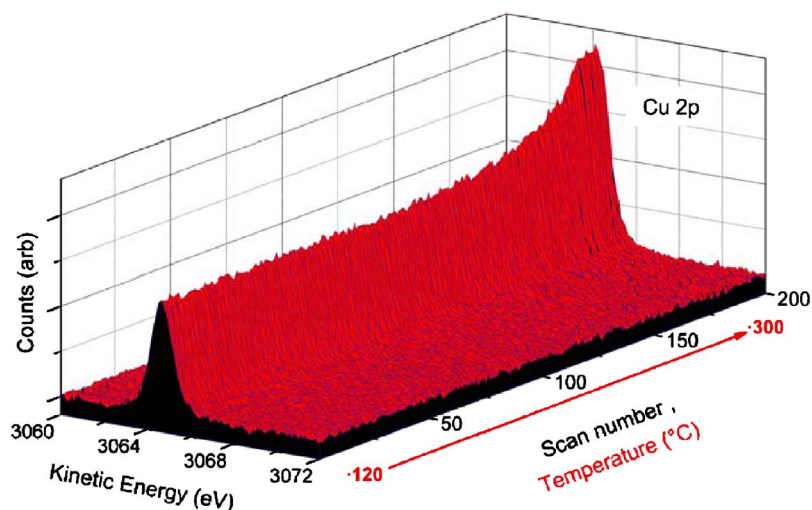


FIG. 16. (Color online) The Cu 2p signal as measured at 4 keV excitation energy during the heating of a copper containing indium sulfide layer. At a temperature of 270 °C the copper content increases and at this temperature, solar cell performance is known to degrade (Ref. 47).

vacuum conditions up to the experiment, (2) by the use of only three optical elements to minimise reflection losses, (3) by collecting a large horizontal radiation fan with the toroidal premirror (6 mrad acceptance), and (4) the optimization of the crystal optics to the *soft* x-ray range and (5) a beamline focus which is actively stabilized both in position and in intensity by two independent feedback loops.

Capillary optics is provisioned for a further reduction of the focus size down to less than 100 μm .

Concluding, soft x-ray bending magnet beamlines at medium energy storage rings provide good opportunities for HIKE spectroscopy and other applications. Especially, the energy tunability at high resolution—made possible by *in situ* crystal change and by the use of high order radiation—is an exclusive option, since this is normally not available at undulator beamlines on high energy SR facilities, when fixed-energy channel cut monochromators are used.

ACKNOWLEDGMENTS

The close cooperation of many people working on different aspects has contributed to the success of this beamline. We thank the BESSY optics group and in particular Alexei Erko for many fruitful discussions on crystal and beamline optics over many years, Michael Pietsch implemented the control software, Frank Höft and Thomas Zeschke supplied the PID-control software, Karsten Holldack and Martin Fuchs developed the prototype PSD and implemented it successfully into the beamline, Karsten Holldack detected and advised how to suppress the BESSY source and beamline eigenfrequencies for an improved mechanical beam stabilization. Last but not the least, thanks are due to the many users who helped in improving the beamline performance by their ambitious demands on different aspects: Holger Dau and Michael Haumann of FU Berlin implemented a quick and stable EXAFS operation with high data quality. Wolfgang Eberhardt and Walter Braun of BESSY and Svante Svensson of Uppsala University, Sweden promoted strongly the ultrahigh resolution work essential for the HIKE experiment.

- ¹J. Bahrtdt, W. Frentrup, A. Gaupp, P. Kuske, M. Scheer, W. Gudat, G. Ingold, and S. Sasaki, Nucl. Instrum. Methods Phys. Res. A **467–468**, 21 (2001).
- ²M. R. Weiss, R. Follath, K. J. S. Sawhney, F. Senf, J. Bahrtdt, W. Frentrup, A. Gaupp, S. Sasaki, M. Scheer, H.-Ch. Mertins, D. Abramsohn, F. Schaefers, W. Kuch, and W. Mahler, Nucl. Instrum. Methods Phys. Res. A **467**, 449 (2001).
- ³http://www.bessy.de/users_info/02.undulators
- ⁴R. Follath, Nucl. Instrum. Methods Phys. Res. A **467**, 418–425 (2001).
- ⁵R. Follath, F. Senf, and W. Gudat, Space Sci. Instrum. **5**, 769 (1998).
- ⁶http://www.bessy.de/users_info/02.beamlines
- ⁷D. Cocco, A. Bianco, B. Kaulich, F. Schaefers, M. Mertin, G. Reichardt, B. Nelles, and K. F. Heidemann, AIP Conf. Proc. **879-I**, 497 (2007).
- ⁸A. Erko, I. Packe, W. Gudat, N. Abrosimov, and A. Firsov, Nucl. Instrum. Methods Phys. Res. A **467–468**, 623 (2001).
- ⁹E. Dudzik, R. Feyerherm, W. Diete, R. Signorato, and Ch. Zilkens, J. Synchrotron Radiat. **13**, 421 (2006).
- ¹⁰B. R. Müller, W. Görner, M. P. Hentschel, H. Riesemeier, M. Krumrey, G. Ulm, W. Diete, U. Klein, and R. Frahm, Nucl. Instrum. Methods Phys. Res. A **467–468**, 703 (2001).
- ¹¹A. Erko, F. Schaefers, A. Firsov, W. B. Peatman, W. Eberhardt, and R. Signorato, Spectrochim. Acta, Part B **59**, 1543–1548 (2004).
- ¹²U. Heinemann, K. Büsow, U. Mueller, and P. Umbach, Acc. Chem. Res.

- 36**, 157 (2003).
- ¹³B. Jenichen, W. Braun, V. M. Kaganer, A. G. Shtukenberg, L. Däweritz, C.-G. Schulz, K. H. Ploog, and A. Erko, Rev. Sci. Instrum. **74**, 1267 (2003).
- ¹⁴J. Feldhaus, F. Schaefers, and W. Peatman, Proc. SPIE **733**, 242 (1987).
- ¹⁵J. Wong, Z. U. Rek, M. Rowen, T. Tanaka, F. Schaefers, B. R. Müller, G. N. George, I. J. Pickering, G. H. Via, B. DeVries, G. E. Brown, and M. Fröba, Physica B **208&209**, 220 (1995).
- ¹⁶J. Wong, T. Tanaka, M. Rowen, F. Schaefers, B. R. Mueller, and Z. U. Rek, J. Synchrotron Radiat. **6**, 1086 (1999).
- ¹⁷E. Holmström, W. Olovsson, I. A. Abrikosov, A. M. N. Niklasson, B. Johansson, M. Gorgoi, O. Karis, S. Svensson, F. Schaefers, W. Braun, G. Öhrwall, G. Andersson, M. Marcellini, and W. Eberhardt, Phys. Rev. Lett. **97**, 266106 (2006).
- ¹⁸A. Sekiyama and S. Suga, J. Electron Spectrosc. Relat. Phenom. **137–140**, 681 (2004).
- ¹⁹Y. Takata, M. Yabashi, K. Tamasaku, Y. Nishino, D. Miwa, T. Ishikawa, E. Ikenaga, K. Horiba, S. Shin, M. Arita, K. Shimada, H. Namatame, M. Taniguchi, H. Nohira, T. Hattori, S. Soedergren, B. Wannberg, and K. Kobayashi, Nucl. Instrum. Methods Phys. Res. A **547**, 50 (2005).
- ²⁰G. Panaccione, G. Cautero, M. Cautero, A. Fondacaro, M. Griioni, P. Lacovig, G. Monaco, F. Offi, G. Paolicelli, M. Sacchi, N. Stojic, G. Stefani, R. Tommasini, and P. Torelli, J. Phys.: Condens. Matter **17**, 2671 (2005).
- ²¹S. Thiess, C. Kunz, B. C. C. Cowie, T.-L. Lee, M. Reniera, and J. Zegenhagen, Solid State Commun. **132**, 589 (2004).
- ²²F. Schaefers, in: *Modern Developments in X-Ray and Neutron Optics*, edited by A. Erko, M. Idir, Th. Krist, and A. G. Michette (Springer, Berlin, 2007).
- ²³A. Erko, I. Packe, W. Gudat, N. Abrosimov, and A. Firsov, Nucl. Instrum. Methods Phys. Res. A **467–468**, 358 (2001).
- ²⁴M. Krumrey and G. Ulm, Nucl. Instrum. Methods Phys. Res. A **467–468**, 1175 (2001).
- ²⁵M. Krumrey and E. Tegeler, Rev. Sci. Instrum. **63**, 797 (1992).
- ²⁶J. Feldhaus, BESSY Technischer Bericht TB **44**, 1 (1983).
- ²⁷S. Doniach and M. Sunjic J. Phys. C **3**, 285 (1970).
- ²⁸L. Lindau, P. Pianetta, S. Doniach, and W. E. Spicer, Nature (London) **250**, 214 (1974).
- ²⁹Within a joint project between BESSY and Free University Berlin (EC-FP6 integrated project BIOXHIT), <http://www.bioxhit.org>, and partners from several European Storage Rings (BESSY, DESY, DIAMOND, ESRF, and SOLEIL).
- ³⁰Micron Semiconductor Ltd, Lancing, UK, <http://micronsemiconductor.co.uk>
- ³¹M. R. Fuchs, K. Holldack, F. Schaefers, F. Höft, and U. Mueller, BESSY annual report 2006, pp. 216–218 (to be published).
- ³²A. Magnuson, P. Liebisch, J. Höglblom, M. Anderlund, R. Lomoth, W. Meyer-Klaucke, M. Haumann, and H. Dau, J. Inorg. Biochem. **100**, 1234 (2006).
- ³³M. Barra, M. Haumann, R. Krivanek, P. Loja, A. Grundmeier, and H. Dau, Biochemistry **45**, 14523 (2006).
- ³⁴S. Löscher, L. Schwartz, M. Stein, S. Ott, and M. Haumann, “Facilitated hydride binding in an Fe-Fe hydrogenase active-site biomimic revealed by X-ray absorption spectroscopy and DFT calculations,” Inorg. Chem. (in press) (2007).
- ³⁵H. Dau, A. Grundmeier, P. Loja, and M. Haumann, “On the structure of the manganese complex of photosystem II—Extended-range EXAFS data and specific atom-resolution models for four S-states,” Philos. Trans. R. Soc. London, Ser. B (2007).
- ³⁶B. D. Beake, V. M. Vishnyakov, R. Valizadeh, and J. S. Colligon J. Phys. D **39**, 1392 (2006).
- ³⁷Y. G. Shen, Z. J. Liu, N. Jiang, H. S. Zhang, K. H. Chan, and Z. K. Xu, J. Mater. Res. **19**, 523 (2004).
- ³⁸F. Vaz, L. Rebouta, Ph. Goudeau, T. Girardeau, J. Pacaud, J. P. Riviere, and A. Traverse, Surf. Coat. Technol. **146–147**, 274 (2001).
- ³⁹J. L. Endrino and J. E. Krzanowski, J. Mater. Res. **7**, 3163 (2002).
- ⁴⁰J. L. Endrino, S. Palacín, A. Gutiérrez, M. Aguirre, and F. Schaefers, *Materials Research Society Symposia Proceedings* (Materials Research Society, Pittsburgh, 2007), Vol. 976, Paper No. EE03-18.
- ⁴¹J. L. Endrino, S. Palacín, M. H. Aguirre, A. Gutiérrez, and F. Schaefers, Acta Mater. **55–56**, 2129 (2007).
- ⁴²W. Drube, Th. Eickhoff, H. Schulte-Schrepping, and J. Heuer, AIP Conf. Proc. **705**, 1130 (2004).

- ⁴³K. Kobayashi, M. Yabashi, Y. Takata, T. Tokushima, S. Shin, K. Tamasaki, D. Miwa, T. Ishikawa, H. Nohira, T. Hattori, Y. Sugita, O. Nakatsuka, A. Sakai, and S. Zaima, *Appl. Phys. Lett.* **83**, 1005 (2003).
- ⁴⁴M. Gorgoi, S. Svensson, F. Schaefers, G. Öhrwall, M. Mertin, P. Bressler, O. Karis, H. Siegbahn, W. Doherty, C. Jung, W. Braun, and W. Eberhardt, *Nucl. Instrum. Meth.* (in press).
- ⁴⁵E. M. J. Johansson, C. Platzer-Björkman, H. Rensmo, A. Sandell, H. Siegbahn, L. Stolt, M. Gorgoi, S. Svensson, E. Lewin, F. Schaefers, W. Braun, and W. Eberhardt, BESSY annual report, 2006, pp. 508–509 (to be published).
- ⁴⁶I. Laueremann, Ch. Loreck, A. Grimm, R. Klenk, H. Mönig, M. Ch. Lux-Steiner, Ch.-H. Fischer, S. Visbeck, and T. P. Niesen, *Thin Solid Films* **515**, 6015 (2007).
- ⁴⁷I. Laueremann, P. Pistor, A. Grimm, B. Johnson, T. Kropp, M. Ch. Lux-Steiner, H. Mönig, R. Klenk, Ch.-H. Fischer, M. Gorgoi, W. Braun, and F. Schaefers (to be published).